LLNL-JRNL-408459

Identifying Isotropic Events Using a Regional Moment Tensor Inversion

S. R. Ford, D. S. Dreger, W. R. Walter

November 6, 2008

Journal of Geophysical Research

Disclaimer

Identifying isotropic events using a regional moment tensor inversion

Sean R. Ford [a,b], Douglas S. Dreger [a], William R. Walter [b]

[a] Berkeley Seismological Laboratory, Berkeley, California-94720, USA

[b] Lawrence Livermore National Laboratory, Livermore, California-94550, USA

Abstract

We calculate the deviatoric and isotropic source components for 17 explosions at the Nevada Test Site, as well as 12 earthquakes and 3 collapses in the surrounding region of the western US, using a regional time-domain full waveform inversion for the complete moment tensor. The events separate into specific populations according to their deviation from a pure double-couple and ratio of isotropic to deviatoric energy. The separation allows for anomalous event identification and discrimination between explosions, earthquakes, and collapses. Confidence regions of the model parameters are estimated from the data misfit by assuming normally distributed parameter values. We investigate the sensitivity of the resolved parameters of an explosion to imperfect Earth models, inaccurate event depths, and data with low signal-to-noise ratio (SNR) assuming a reasonable azimuthal distribution of stations. In the band of interest (0.02-0.10 Hz) the source-type calculated from complete moment tensor inversion is insensitive to velocity models perturbations that cause less than a half-cycle shift (<5 sec) in arrival time error if shifting of the waveforms is allowed. The explosion source-type is insensitive to an incorrect depth assumption (for a true depth of 1 km), and the goodness-of-fit of the inversion result cannot be used to resolve the true depth of the explosion. Noise degrades the explosive character of the result, and a good fit and accurate result are obtained when the signal-to-noise ratio (SNR) is greater than 5. We assess the depth and frequency dependence upon the resolved explosive moment. As the depth decreases from 1 km to 200 m, the isotropic moment is no longer accurately resolved and is in error between 50-200%. However, even at the most shallow depth the resultant moment tensor is dominated by the explosive component when the data have a good SNR.

1. Introduction

The full seismic moment tensor (2nd rank tensor, M_{ij}) is a general representation of any seismic point source in terms of force-couples (Gilbert, 1971), and is used in tectonic studies to describe the double-couple (DC) nature of shear-faulting. However, M_{ij} is sufficiently general to represent non-DC seismic sources (for an outstanding review of non-DC earthquakes, see Julian et al., 1998). The isotropic component of the moment tensor ($M_{ij}^{\mathrm{ISO}} = \delta_{ij}\,(M_{11}+M_{22}+M_{33})/3$) is related to the volume change associated with a source (Muller, 1973), and is significant in the case of an explosion. The deviatoric component of M_{ij} ($M_{ij}^{\mathrm{DEV}} = M_{ij} - \delta_{ij}\,(M_{11}+M_{22}+M_{33})/3$) is most often employed to define the DC source, but can also describe the volume-compensated linear vector dipole (CLVD), which has been used to explain deep seismicity (e.g., Knopoff and Randall, 1970; Kawakatsu, 1990), and has also been shown to result from complex faulting events (Kuge and Lay, 1994). Complex sources like a tensile crack require a combination of deviatoric and isotropic components, and the opening-crack has been suggested as a source for some volcanic events (e.g., Foulger et al., 2004; Templeton and Dreger, 2006) and the closing-crack for mine collapses (e.g. Pechmann et al., 1995; Bowers and Walter, 2002).

The inversion of seismic data to calculate the deviatoric moment tensor has been done for over 30 years in both the time-domain (e.g., Stump and Johnson, 1977) and frequency domain (e.g., Gilbert and Dziewonski, 1975). The inversion of full-waveform data from regional events is now routine practice at several institutions including the Berkeley Seismological Laboratory since 1993 (Romanowicz et al., 1993), where the results are housed at the Northern California Earthquake Data Center (NCEDC; www.ncedc.org/ncedc/mt.html). Recently, Minson and

Dreger (2008) have extended the full-waveform inversion to calculate all six independent elements of the symmetric moment tensor, which allows for estimation of the isotropic component of the source.

The concept of using intermediate period waveforms, particularly surface wave radiation patterns, to identify explosions goes back more than 40 years. Early results were disappointing due to the presence of unexpected Love waves and occasional reversed Rayleigh waves from tectonic release (e.g. Press and Archambeau, 1962; Brune and Pommery, 1963). However despite these complexities, the well-established ratio of surface wave magnitude (M_S) to body wave magnitude (m_b) separates earthquakes from explosions even when there is significant tectonic release, indicating there are differences in the waveforms, even if the explosion signals do not always conform to the simple isotropic model. Identification of events with demonstrably significant isotropic components can aid in yield determination (e.g., Stevens and Murphy, 2001; Patton, 1991) and possibly nuclear test discrimination (e.g., Woods et al., 1993). Given and Mellman (1986) inverted teleseismic long-period fundamental mode surface waves from 18 large ($m_b \geq 5.5$) nuclear test explosions at the Nevada Test Site (NTS) to calculate a three-parameter source model. The model was used to estimate the isotropic moment (M_I), along with the strike and moment of an assumed vertical strike-slip component, and they found no improvement in yield estimation when using M_I as opposed to M_S. Patton (1988) added higher mode Rayleigh wave data from stations at regional distances and performed an inversion for the full moment tensor with an additional directed force component to represent spall for the HARZER explosion (m_b5.6) at NTS. The study was later extended to 16 nearby explosions and the relationship between total seismic moment (M_0) and yield agreed well with previous results using M_S (Patton, 1991). Dreger and Woods (2002) examined three NTS nuclear tests using data from three TERRAscope stations in southern California (180° < azimuth < 230°). The work presented here amends and extends their study to 14 more nuclear tests at the NTS, three collapses (two mine collapses and one explosion cavity collapse), and 12 earthquakes near the NTS (Figure 1; Table 1).

2. Data and Method

We implement the time-domain full-waveform inversion of regional data for the complete moment tensor devised by Minson and Dreger (2008) after Herrmann and Hutcheson (1993) based on the work of Langston (1981). In general, synthetic seismograms are represented as the linear combination of fundamental Green's functions where the weights on these Green's functions are the individual moment tensor elements. The Green's functions for a one-dimensional (1-D) velocity model of eastern California and western Nevada (Table 2; Song et al., 1996) are calculated as synthetic displacement seismograms using a frequency-wavenumber integration method (Saikia, 1994). The synthetic data are filtered with a 4-pole acausal Butterworth filter with a low-corner of 0.02 Hz and a high-corner of 0.05 Hz and 0.1 Hz for events with $M_W \geq 4$ and $M_W < 4$, respectively. At these frequencies, where dominant wavelengths are tens of kilometers, we assume a point source for the low-magnitude regional events investigated in this study. The point source assumption allows for linearization in the time-domain, which is where we carry out the least-squares inversion.

We analyzed events that were digitally recorded with a high signal-to-noise ratio by more than two regional broadband stations. Three-component data were collected from a total of 52 stations from the US National Seismic Network, IRIS/USGS, Berkeley Digital Seismic Network, Trinet, and the Lawrence Livermore National Laboratory (LLNL) network (Figure 1; Supplemental Table 1). All data are freely available from IRIS via the internet except the LLNL historic network data, which is available on compact disk (Walter et al., 2004). Not all stations recorded all events, and a total of 16 stations were used in the inversion of the explosion data, which are listed in Figure 1. We remove the instrument response, rotate to the great-circle frame, integrate to obtain displacement, and use the same filter as for the synthetic seismograms. The LLNL network (white triangles in Figure 1) was composed of Sprengnether instruments with limited long-period response, and for those data we used a passband of 10 - 30 seconds for both the data and synthetics.

We calibrated the algorithm by calculating the full moment tensor for the 1992 Little Skull Mountain event (Figure 1). We find a solution at all depths within 5 km of the reported depth. The depth that produces Green's functions that best fit the data is used in the final solution. Fit is quantified by the variance reduction (VR), which is a normalized variance given by

$$\mathrm{VR} = \left[1 - \frac{\sum_i (d_i - s_i)^2}{\sum_i d_i^2} \right] \times 100 , \qquad (1)$$

where *i* are the displacements at all times for all components at all stations, and *d*, and *s* are the data and synthetic respectively..

We also allow the Green's functions calculated at a given distance to shift relative to the data to address small hypocentral errors and uncertainty in the velocity model used to compute the Green's functions. The shift that produces the best fit is used in the final solution. We limit the shift to less than 5 and 3 sec for high-pass corners of 0.05 and 0.10 Hz, respectively. The allowed time shift is large enough to make up for small hypocentral errors, but small enough to disallow cycle-skipping that could produce erroneous mechanisms. The sensitivity of the time shift relative to the assumed velocity model will be discussed later in the paper. The full moment tensor solution is decomposed to an isotropic and deviatoric component in Figure 2a. We calculate the total scalar moment (M_0) as defined by Bowers and Hudson (1999), where M_0 is equal to the sum of the isotropic moment ($M_{ISO} = (M_{11}+M_{22}+M_{33})/3$) and deviatoric moment (M_{DEV}), which is the largest deviatoric eigenvalue. For the Little Skull Mountain event we find $M_0 = 3.7 \times 10^{17}$ N-m ($M_W = 5.6$), and the solution has a negligible isotropic moment ($M_{ISO} = -0.31 \times 10^{17}$ N-m) so there is little change between the full and deviatoric solutions. The solution fits the data very well (Figure 2b) and is similar to the double-couple solution of Walter (1993), the deviatoric solution of Ichinose et al. (2003), and the full solution of Dreger and Woods (2002).

With the same algorithm we calculate the full moment tensors of 17 nuclear test explosions at the NTS (Figure 1). In the case of explosions and collapses we calculate Green's functions at a depth of 1 km. The sensitivity of this assumption will be investigated later in the paper. An example of the analysis is given by the solution for the 1991 HOYA test in Figure 3, where both the full and deviatoric moment tensors are given. The largest component in the decomposition is isotropic and it contributes 70% of the total scalar moment.

3. Results

It is difficult to grasp the source-type from the standard focal mechanism plot for events with a large non-DC component. For example, one cannot discern the relative contributions of the isotropic and deviatoric components from the full focal mechanism in Figure 3 for the HOYA explosion. In order to get at the tectonic contribution to the explosion, one could separate the deviatoric component into a DC and a CLVD that share the orientation of the major axis, but decompositions of this type are non-unique, where for example the DC and CLVD decomposition could be replaced by two DCs (see Julian et al. (1998) for further decompositions). In an attempt to better characterize mechanisms we follow the source-type analysis described in Hudson et al. (1989) and calculate -2ε and k, which are given by

$$\varepsilon = \frac{-m_1'}{|m_3'|}, \tag{2}$$

and

$$k = \frac{M_{\mathrm{ISO}}}{|M_{\mathrm{ISO}}| + |m_3'|}, \tag{3}$$

where m'_1, m'_2 and m'_3 are the deviatoric principal moments for the N, P, and T axes, respectively, and $|m'_1| \leq |m'_2| \leq |m'_3|$. ε is a measure of the departure of the deviatoric component from a pure DC mechanism, and is 0 for a pure double-couple and ±0.5 for a pure CLVD. k is a measure of the volume change, where +1 would be a full explosion and –1 a full implosion. -2ε and k for the Little Skull Mountain earthquake and NTS explosion, HOYA, are given in Figure 4a. The earthquake is almost at the origin, which defines a pure DC, whereas the nuclear test is near where a theoretical explosion would plot. In order to estimate formal error in the fit, we create moment tensor populations by bootstrapping the residuals of the fit $n$times with replacement and then use those populations of size n to calculate -2ε and k, resulting in their own populations to which we fit normal distributions. Figure 4a shows the population of n = 1000 along with the 95% confidence region for the DIVIDER explosion. Increasing n resulted in no change to the confidence regions.

Hudson et al. (1989) transform the parameters -2ε and k so that the displayed plot will have equal normal probability areas based on the assumption that the smallest principal moments can take any value between ± the largest absolute principal moment (Julian et al., 1998). The plot derived this way is the source-type plot and it is shown in Figure 4b for the parameters from the Little Skull Mt. earthquake and HOYA explosion. Figure 4b also shows the transformed bootstrap population for the DIVIDER explosion and its associated 95% confidence region. The transformation makes the assumption of normality in the error distribution valid as can be seen by the improved fit of an error ellipse to the bootstrap population between Figure 4a and b. The Hudson et al. (1989) plot is a superior way to display source-type and analyze error in the parameters. The error ellipses are not shown for the Little Skull Mt. earthquake or HOYA explosion examples because the error regions are too small to notice a difference due to the transformation.

We carry out similar analyses for 11 more earthquakes and three collapses (one cavity and two mine) and produce the source-type plot in Figure 5 along with the 95% confidence regions. The nuclear tests occupy the region where $k > 0.5$, the earthquakes cluster near the origin, and the collapses plot almost exactly at (1,-5/9), which is the location for a closing crack in a Poisson solid. Deviations from these trends will be discussed later. Moment tensor elements and source-type parameters for all events are given in Table 3.

4. Sensitivity Analysis

The relatively small area of the confidence regions given in Figure 5 and the excellent synthetic seismogram fit to the data as quantified by VR gives us great confidence that the assumed velocity model and depth are correct and the estimated moment tensor solutions are robust. However, these measures of goodness-of-fit assume the underlying model used to invert the data is correct. In the following section we will test these assumptions with synthetic data from a theoretical explosion ($-2\varepsilon=0$, $k=1$) created for two experimental geometries. The first geometry, referred to as ‘Ideal’, is eight stations at distance increments between 100 and 300 km each separated by 45° in azimuth. The second station geometry mirrors the analysis for the HOYA explosion. The station distributions are given in Figure 6. The synthetic data are filtered in the same two bands (20-50s and 10-50s) used in the analysis and when combined with the two geometries results in 4 scenarios.

4.1. Noise

The error analysis presented above is due to misfit of the data by the least-squares inversion. Part of the misfit may be due to nonstationary noise and we test the sensitivity of the inversion to different signal-to-noise ratios (SNR). In order to best approximate real-world noise conditions, we derive the noise signal from data prior to the first arrival from the nuclear test METROPOLIS (10 Mar 90) at station ANMO for all three components. The amplitude of this noise signal is bandpassed to match the synthetic data and multiplied by a factor so as to create a final synthetic signal with the desired SNR (ratio of synthetic data root-mean-square amplitude to noise root-mean-square amplitude).

The noise analysis has very little frequency dependence so for clarity we only show results from the analysis in the 20 - 50 sec frequency band in Figure 7a. The Ideal configuration produces the best scenario where a large k is retrieved (>0.3) when the SNR is greater than 2. For all scenarios $k > 0.5$ when SNR > 5. Typically, we use data with an SNR greater than 10, however there are a few cases where the SNR is close to 3. An example of this type of data is given in Figure 8 for the DIVIDER explosion, which produced signal that was right on the limit of acceptable SNR (see stations ELK and MHC) but still produced a well-fit solution.

4.2. Incorrect Depth

Another source of error not incorporated into the formal error analysis is incorrectly calculated Green's functions due to ignorance of the true event depth. The method that produces the results presented above attempts to find an optimal depth for the earthquakes by perturbing the reported depth a few kilometers, performing the inversion, and finding the best-fit solution. For all explosions and collapses the depth is fixed at 1 km. If this method were to be used for an event with an unknown source type, the depth could be an important source of error, as well as an important parameter for identification. We perform another synthetic test in which an explosion at 1 km is inverted with Green's functions calculated at varying depths.

The source depth analysis is not greatly affected by the two station configurations considered here, therefore we only show results for the HOYA configuration in Figure 7b. The result at an incorrect depth of 2 km is virtually indistinguishable from the true answer. When the source is moved to 3 km depth there is a small step decrease in k due to a layer in the velocity model that begins at 2.5 km depth. However, $k > 0.5$ for incorrect depths < 17 km with slightly more sensitivity in k and worse fit in the high frequency band (10 - 50 sec) compared to the low frequency band (20 - 50 sec). The relative insensitivity of the solution to mislocated depth for an explosion is different than is observed for DC events. Dreger and Woods (2002) show that the VR of the Little Skull Mountain earthquake solution is definitively maximized at the assumed true event depth. Thus while the depth sensitivity of explosions is poor, the method is able to determine depth of non-explosion sources, which also provides an important level of event screening.

4.3. Velocity Model

Finally, we test how error in the assumed Earth structure is mapped through the Green's functions to error in the solution. We start with the well-calibrated Song et al. (1996) velocity model (Table 2) and perturb the velocities and depths of the layers using averaged parameters from another plausible velocity model (WestUS; Ammon, 1999) and a model from Southern California (SoCal; Dreger and Helmberger, 1990). Perturbed values are given in Table 4, which result in a population of 243 models.

In order to produce a sensitivity test that best mimics our analysis, we use the time shift rule to filter the models. This means that we only allow velocity models that produce Green’s functions where the time shift between data and synthetics that produces the best-fit solution is less than or equal to 5 or 3 sec from the theoretical arrival time for high-pass corners of 0.05 or 0.10 Hz, respectively. Primarily due to the velocity model filtering there is little difference among the scenarios so we only show source-type plots for the HOYA configuration in the 20 - 50 sec frequency band in Figure 7c. For this scenario the number of acceptable models is reduced to 88, and although not all possible combinations of model parameters are used, each parameter perturbation given in Table 4 is employed at least once.

Without shifting there are a few velocity models that produce well-fit solutions (VR>90%) with mechanisms that are almost purely DC. However, when shifting is allowed all velocity models produce good fits with highly explosive sources (*k*~>0.4).

4.4. Free-surface effects

Another consideration is the ability to resolve displacements for explosions near the surface. Since tractions normal to the vertical vanish at the free surface, the excitation coefficients associated with those tractions must vanish (Julian et al., 1998). Therefore at the free surface the moments of M_{13}, M_{23}, and the isotropic part of the M_{ij} cannot be resolved. Given and Mellman (1986) showed that at a source depth of 1 km the fundamental mode excitation functions associated with the moments listed previously effectively go to zero. We investigate the potential problems associated with vanishing traction at the free surface by inverting noisy data from a synthetic explosion source at depths between 200 and 1000 m in a three-layer 1D velocity model using Green's functions calculated at those same depths.

The ability to resolve an explosive component is dependent on the station distribution, frequency and SNR of the analysis, therefore Figure 9 shows all 4 scenarios. An explosive component (k>0.5) can be resolved under favorable noise conditions at a depth greater than 300 m for all scenarios, though with error in M_{ISO} between 50-150% (Figure 9a-d). The error is inversely proportional to the depth. For all scenarios, but the HOYA configuration at 20-50 sec (Figure 9a), favorable noise means SNR $\geq$ 6. The change in M_{ISO} is due to a change in M_{33} relative to the other dipole components (Figure 9i-p), and this produces an erroneous deviatoric component. The moment of deviatoric component can be up to 50% of the theoretical isotropic moment (Figure 9e-h) and since it is related to the error in M_{ISO} it is inversely proportional to the depth. At less than 200 m depth, the synthetic displacements become too small and the solution using these particular Green's functions is unreliable.

5. Discussion

The populations of earthquakes, explosions, and collapses separate in the source-type plot. These initial results are very encouraging and suggest a discriminant that employs the source-type plot parameters (-2ε, k). Another advantage of the source-type plot is its display of 2-D error regions. In this way one can test a hypothesis that an event has a non-DC component. For example, the earthquake that is furthest to the top-left in Figure 5 is the Frenchman Flat earthquake. The least-squares error analysis allows one to state that the event is significantly non-DC at the 95% confidence level and it plots near the theoretical opening crack. The Frenchman Flat event was also analyzed by Ichinose et al. (2003) and found to be non-DC as well.

The source-type analysis can also be utilized to estimate model-based error as well. The error introduced by ignorance of the event location and Earth structure can be calculated with a Monte Carlo approach, where several solutions are computed for a priori distributions of the hypocentral location and Earth model obtained from independent analyses. For example, confidence regions for a given hypocentral location as published by the NEIC can act as the a priori location distribution and the hundreds of 1-D velocity models for a given region produced from a Markov Chain Monte Carlo method as in Pasyanos et al. (2006) can act as the velocity model distribution. Each of the moment tensor solutions could then be plotted producing a scatter density, which would aid in the understanding of how parameterization choice nonlinearly affects the moment tensor solutions, and help map the solution space of best-fit moment tensors.

We try to give some insight to the depth sensitivity of the method with Figure 7b. In previous analyses of crustal earthquakes, the goodness-of-fit (VR) peaks at the correct depth (Dreger and Woods, 2002). If the same behavior is true of explosions, then the method could act as a discriminant if the best depth is very shallow which is atypical of earthquakes. Of course the alternative is also helpful, if an event solution shows the event to be in the typical range of earthquakes, greater than several km then the estimate provides a level of screening if not discrimination. Figure 7b shows that the use of this method as a precise depth discriminant is not plausible for the frequencies used here, though sensitivity does increase for the higher frequency band.

These results are a demonstration of the fact that an isotropic radiation pattern has no sensitivity to takeoff angle, which depends on depth. As shown by Dreger and Woods (2002) there is limited resolution of the shallow depth of explosions using regional distance data. Although an explosive radiation pattern alone does not have depth sensitivity, the relative excitation of low frequency body waves (Pnl) and Rayleigh waves does enable the method to discern the relatively shallower depths of explosions compared to earthquakes.

The velocity model analysis shown in Figure 7c suggests that the maximum shift rule used in the analysis is a good proxy for evaluating the appropriateness of the velocity model. The level of departure of a given velocity model from the true model is station distribution, frequency, and SNR dependent. Therefore, it is a good idea to perform this style of sensitivity test to evaluate the amount of deviation a certain experimental setup will allow, because if the velocity model is poorly calibrated then a good fit to the data can be obtained but the solution may be inaccurate.

Sileny (2004) investigated the sensitivities of the deviatoric solution and found that velocity perturbations of more than 30% and event depths mislocated by two times the actual depth still return an accurate solution. A further consideration is the assumption of an isotropic Earth structure in the presence of anisotropic data, which may produce a spurious CLVD component (Sileny and Vavrycuk, 2002). Fortunately, the 1-D velocity model seems to be a good approximation in the presence of smoothly varying 3-D heterogeneity (Panning et al., 2001) for the frequency band and regional distances employed here.

The change in moment due to the loss of traction at the free surface affects yield estimation, though event discrimination is still reliable at high SNR. A result of this change in moment is that the deviatoric moment becomes non-zero and could be significant at very shallow depths ($Z<500$ m) and low SNR ($SNR<6$). The moment manifests as a CLVD component, which means that interpretation of non-isotropic energy may be flawed for shallow events even with high SNR data. Though as Figure 9 suggests this effect is station configuration, frequency, and SNR dependent. There is quite a difference in M_{ISO} determined for different frequency bands for the HOYA configuration (Figure 9a-b), whereas there is only a slight difference for the Ideal configuration (Figure 9c-d). Also, the high frequency scenario of the HOYA configuration is relatively less sensitive to low SNR than other scenarios (Figure 9b).

The explosions analyzed here do not have as much non-isotropic energy as has historically been observed at NTS and in other regions (Walter and Patton, 1990; Ekstrom and Richards, 1994). This may be due to the "wearing out" of the test site over time (Aki and Tsai, 1972), so future work will expand the dataset of explosions to encompass other regions exhibiting exotic records like the "reversed" Rayleigh waves observed for the 1998 Indian tests (Walter and Rodgers, 1999). Future work will also address more challenging station configurations and noise considerations as is commonly found in recent nuclear tests. As shown in this study, a robust constraint on the isotropic component is station configuration, signal bandwidth, and data-quality dependent. Therefore, future work will test the extent to which an isotropic component can be resolved and believed for specific previous and potential future test scenarios.

6. Conclusions

Nuclear test explosions from NTS and earthquakes from the surrounding region separate into specific populations according to source-type parameters, which are based on relative magnitudes of isotropic and deviatoric moments. The separation allows for anomalous event identification and discrimination between explosions, earthquakes, and collapses. Synthetic tests show that a mislocation in depth and small deviations in a simple 1D velocity model still recover a significant isotropic component, though Earth complexity is inadequately represented by a three-layer structure. We also assess error due to vanishing traction at the free surface and are able to resolve a reliable mechanism at depths greater than 300 m for data with a good SNR.

7. Acknowledgements

We thank Jeff Stevens for discussions regarding free surface effects and Howard Patton for insights on the CLVD contribution to the explosion source. We are grateful for reviews from

Thorne Lay and Associate Editor, Felix Waldhauser. Figures were made with Generic Mapping Tools (Wessel and Smith, 1998) and the script to make the source-type plots is from Bruce Julian. This is LLNL contribution # and BSL contribution #. This research is sponsored by the National Nuclear Security Administration, contract #DE-FC52-06NA27324

8. References

Aki, K. and Y.-B. Tsai (1972). Mechanism of love-wave excitation by explosive sources, J. Geophys. Res., 77(8), 1452-1475.

Bowers, D and W. R. Walter, (2002), Discriminating between large mine collapses and explosions using teleseismic P waves, *Pure. Appl. Geophys., 159*, 803-830.

Bowers, D. and J.A. Hudson (1999). Defining the scalar moment of a seismic source with a general moment tensor, Bull. Seis. Soc. Amer., 89(5), 1390-1394.

Brune, J. N. and P. Pomeroy (1963). Surface wave radiation for underground nuclear explosions and small magnitude earthquakes, J. Geophys. Res. 68, 5005-5028.

Dreger, D. S. and D. V. Helmberger (1990), Broadband modeling of local earthquakes, Bulletin of the Seismological Society of America, 80, 1162-1179.

Dreger, D. and B. Woods (2002). Regional distance seismic moment tensors of nuclear explosions; seismic source mechanism through moment tensors, Tectonophysics, 356(1-3), 139-156.

Ekstrom, G. and P.G. Richards (1994). Empirical measurements of tectonic moment release in nuclear-explosions from teleseismic surface-waves and body waves, Geophys. J. Int., 117(1), 120-140.

Foulger, G. R., B. R. Julian, D. P. Hill, A. M. Pitt, P. E. Malin, and E. Shalev (2004), Non-double-couple microearthquakes at Long Valley caldera, California, provide evidence for hydraulic fracturing, J. Volcanol. Geotherm. Res., 132, 45-71.

Gilbert, F. (1971), Excitation of the normal modes of the earth by earthquake sources, The Geophysical Journal of the Royal Astronomical Society, 22, 223-226.

Given, J. W. and G.R. Mellman (1986). Estimating explosion and tectonic release source parameters of underground nuclear explosions from Rayleigh and Love wave observations, Tech. rep., Sierra Geophysics Report No. SGI-R-86-126, Kirkland, WA.

Herrmann, R. B. and K. Hutchensen (1993). Quantification of MLg for small explosion, Tech. rep., Phillips Laboratory Report PL-TR-93-2070.

Hudson, J. A., R. G. Pearce, R. G., and R. M. Rogers (1989). Source type plot for inversion of the moment tensor, J. Geophys. Res., 9(B1), 765-774.

Ichinose, G. A., J. G. Anderson, K. D. Smith and Y. Zeng (2003). Source parameters of Eastern California and Western Nevada earthquakes from regional moment tensor inversion, Bull. Seis. Soc. Amer., 93(1), 61-84.

Julian, B. R., A. D. Miller and G. R. Foulger (1998). Non-double-couple earthquakes; 1. Theory, Rev. Geophysics, 36(4), 525- 549.

Kawakatsu, H. (1991), Insignificant isotropic component in the moment tensor of deep earthquakes, Nature (London), 351, 50-53.

Knopoff, L. and M. J. Randall (1970). The compensated linear-vector dipole; a possible mechanism for deep earthquakes, J. Geophys. Res., 75(26), 4957-4963.

Kuge, K. and T. Lay (1994), Systematic non-double-couple components of earthquake mechanisms; the role of fault zone irregularity, J. Geophys. Res., 99(B8), 15,457-15,467.

Langston, C. A. (1981). Source inversion of seismic waveforms; the Koyna, India, earthquakes of 13 September 1967, Bull. Seis. Soc. Amer., 71(1), 1-24.

Minson, S. and D. Dreger (2007). Improved seismic moment tensor inversion, Geophys J. Int..

Muller, G. (1973). Seismic moment and long-period radiation of underground nuclear explosions, Bull. Seis. Soc. Amer., 63(3), 847-857.

Panning, M., D. Dreger and H. Tkalcic (2001). Near-source velocity structure and isotropic moment tensors; a case study of the long valley caldera, Geophys. Res. Lett., 28(9), 1815-1818.

Pasyanos, M. E., G. A. Franz and A. L. Ramirez (2006). Reconciling a geophysical model to data using a Markov Chain Monte Carlo algorithm: An application to the Yellow Sea-Korean Peninsula region, J. Geophys. Res., 111(B3), B03313.

Patton, H. J. (1988). Source models of the Harzer explosion from regional observations of fundamental-mode and higher mode surface waves, Bull. Seis. Soc. Amer., 78(3), 1133-1157.

Patton, H. J. (1991). Seismic moment estimation and the scaling of the long-period explosion source spectrum, in Explosion Source Phenomenology, *American Geophysical Union Monograph, 65,* edited by Taylor, Patton and Richards.

Pechmann, J. C., W. R. Walter, S. J. Nava, and W. J. Arabasz (1995). The February 3, 1995 ML 5.1 seismic event in the trona mining district of southwestern Wyoming, *Seism. Res. Lett., 66*, 25-34.

Press, F. and C. Archambeau (1962). Release of tectonic strain by underground nuclear explosions, *J. Geophys. Res. 67*, 337-343.

Riedesel, M. and T. H. Jordan (1989). Display and assessment of seismic moment tensors, Bull. Seis. Soc. Amer., 79(1), 85-100.

Saikia, C. K. (1994). Modified frequency-wavenumber algorithm for regional seismograms using Filon's quadrature; modelling of Lg waves in Eastern North America, Geophys. J. Int., 118(1), 142-158.

Sileny, J. (2004). Regional moment tensor uncertainty due to mismodeling of the crust, Tectonophysics, 383(3-4), 133-147.

Sileny, J. and V. Vavrycuk (2002). Can unbiased source be retrieved from anisotropic waveforms by using an isotropic model of the medium?; Seismic source mechanism through moment tensors, Tectonophysics, 356(1-3), 125-138.

Song, X. J., D. V. Helmberger and L. Zhao (1996). Broad-band modelling of regional seismograms; the basin and range crustal structure, Geophys. J. Int., 125(1), 15-29.

Springer, D. L., G. A. Pawloski, J. L. Ricca, R. F. Rohrer and D. K. Smith (2002). Seismic source summary for all U.S. below-surface nuclear explosions, Bull. Seis. Soc. Amer., 92(5), 1806-1840.

Templeton, D. C. and D. S. Dreger (2006), Non-double-couple earthquakes in the Long Valley volcanic region, Bulletin of the Seismological Society of America, 96, 69-79.

Toksoz, M. N. and H. H. Kehrer (1972). Tectonic strain release by underground nuclear explosions and its effect on seismic discrimination, Geophys. J. Roy. Aston. Soc., 31(1-3), 141-161.

Vasco, D. W. (1990). Moment-tensor invariants; searching for non-double-couple earthquakes, Bull. Seis. Soc. Amer., 80(2), 354-371.

Walter, W. R. (1993). Source parameters of the June 29, 1992 Little Skull Mountain earthquake from complete regional waveforms at a single station, Geophys. Res. Lett., 20(5), 403-406.

Walter, W. R. and H. J. Patton (1990). Tectonic release from the soviet joint verification experiment, Geophys. Res. Lett., 17(10), 1517-1520.

Walter, W. R., and A. J. Rodgers (1999). Regional waveform modeling in Southwestern Asia; tectonic release from the May 11, 1998 Indian nuclear tests; SSA-99 94th annual meeting; Meeting abstracts, Seismological Research Letters, 70(2), 228.

Walter, W. R., K. D. Smith, J. L. O’Boyle, T. F. Hauk, F. Ryall, S. D. Ruppert, S. C. Myers, R. Abbot and D. A. Dodge (2004). An assembled western United States Dataset for regional seismic analysis, LLNL, UCRL-TR-206630.

Wessel, P., and W. H. F. Smith (1998). New, improved version of generic mapping tools released, in American Geophysical Union, San Francisco, Vol. 79, 579.

Woods, B. B., S. Kedar, and D. V. Helmberger (1993), M (sub L) :M (sub O) as a regional seismic discriminant, Bulletin of the Seismological Society of America, 83, 1167-1183.

Figure 1. Map of the Western US with stations (blue inverted triangles), earthquakes (yellow stars), explosions (red stars), and collapses (green stars) used in this study. The bottom panel is a blow-up of the Nevada Test Site (NTS) region with the NTS outlined in black and in the top panel in red. The top panel also shows the LLNL network (white triangles) and stations used in the explosion analysis (orange triangles). The location of the HOYA test explosion (Figure 3) and Little Skull Mt. earthquake (Figure 2) are also given.

Figure 2. Moment tensor analysis of the 1992 Little Skull Mt. earthquake. a) The full moment tensor elements (in 10^{17} N-m) and mechanism (lower hemisphere projection) are shown along with the deviatoric (DEV) and isotropic (ISO) component. The diameter of the mechanism is related to its relative moment, which is given below the mechanism in N-m.
b) Data (solid grey) compared with synthetic waveforms (dashed black) produced by the full mechanism shown in (a). The station name with azimuth; distance and maximum displacement (cm) are to the left of the data (solid line) and fit (dashed line) produced by inversion in the 20-50 sec passband.

Figure 3. Moment tensor analysis of the 1991 HOYA nuclear test explosion similar to that given in Figure 2 where the moment tensor elements are in 10^{16} N-m. b) Data is bandpassed between 20-50 sec except LAC and MNV (LLNL network) which are bandpassed between 10-30 sec and note that BKS is on a different time scale.

Figure 4. Source-type plot for the Little Skull Mt. earthquake (dark grey circle), NTS test HOYA (light grey diamond), and bootstrap population of the NTS test DIVIDER (black dots) along with

its 95% confidence region (grey ellipse). a) The source-type parameters (k, -2ε) given on a linear plot. b) The source-type plot of Hudson et al. (1989) with theoretical mechanisms plotted as well.

Figure 5. Source-type plot of the 12 earthquakes (blue), 17 explosions (red), 3 collapses (green), and their associated 95% confidence regions (shaded) analyzed in this study. The magnitude of the event is given by the symbol. The abscissa measures the amount of volume change for the source and the ordinate measures the departure from pure DC. Theoretical mechanisms (crosses) are plotted for comparison.

Figure 6. Sensitivity analysis geometry for the HOYA (black triangle) and Ideal (white inverted triangle) station configuration.

Figure 7. Sensitivity analysis. a) Noise is added to the inversion of 20-50 sec synthetic data while velocity model and depth (1 km) are kept fixed for the HOYA (circle) and Ideal (triangle) scenarios. b) The inversion using the HOYA configuration is carried out assuming an incorrect depth while velocity model is kept fixed for data in the 20-50 sec (circle) and 10-50 sec (triangle) band. c) The inversion using the HOYA configuration for 20-50 sec synthetic data is carried out for different three-layer velocity models where the data are not shifted relative to the Green's functions (left panel, circles) and allowed to shift less than 5 sec (right panel, triangles). The symbols are colored as a function of variance reduction (VR).

Figure 8. Moment tensor analysis of the 1992 DIVIDER nuclear test explosion similar to that given in Figure 2 where the moment tensor elements are in 10^{13} N-m. b) Data are bandpassed

between 10-50 sec except KNB and MNV (LLNL network) which are bandpassed between 10-30 sec and note that MHC and WDC are on a different time scale.

Figure 9. Vanishing traction sensitivity. Synthetic data for a pure explosion (k=1) is inverted at depths less than 1 km for varying SNR and the four scenarios discussed in the text. a-d) Resolved M_{ISO} for SNR values of 2 (circle) 6 (inverted triangle) and 10 (triangle) where the value for an inversion without noise (SNR=∞) is given by the black line (100%). k is given by the color. e-h) Resolved M_{DEV} for SNR values of 2 (circle) 6 (inverted triangle) and 10 (triangle) where the total scalar moment for an inversion without noise (SNR=∞) is given by the black line (100%), and M_{DEV} should be 0. -2ε is given by the color. i-l) Moment tensor elements for data with an SNR=10. m-p) Moment tensor elements for data with an SNR=6.

This work performed under the auspices of the U.S. Department of Energy by Lawrence Livermore National Laboratory under Contract DE-AC52-07NA27344.

Table 1. Event list[1]

Name[2]	Date[3]	Time[3]	Latitude[3]	Longitude[3]	Depth (m)[4]	Magnitude[6]
KERNVILLE^{P}	1988/02/15	18:10:00.09	37.314	-116.472	542	5.30_{L}^{NCSN}
AMARILLO^{P}	1989/06/27	15:30:00.02	37.275	-116.354	640	4.90_{L}^{NCSN}
DISKO ELM^{R}	1989/09/14	15:00:00.10	37.236	-116.164	261	4.40_{L}^{NCSN}
HORNITOS^{P}	1989/10/31	15:30:00.09	37.263	-116.492	564	5.40_{L}^{NCSN}
BARNWELL^{P}	1989/12/08	15:00:00.09	37.231	-116.410	601	5.30_{L}^{NCSN}
METROPOLIS^{Y}	1990/03/10	16:00:00.08	37.112	-116.056	469	4.94_{d}^{NCSN}
BULLION^{P}	1990/06/13	16:00:00.09	37.262	-116.421	674	5.34_{d}^{NCSN}
AUSTIN^{Y}	1990/06/21	18:15:00.00	36.993	-116.005	350	4.11_{d}^{NCSN}
HOUSTON^{N}	1990/11/14	19:17:00.07	37.227	-116.372	594	4.86_{d}^{NCSN}
COSO^{Y}	1991/03/08	21:02:45.08	37.104	-116.075	417[5]	4.50_{L}^{NCSN}
BEXAR^{P}	1991/04/04	19:00:00.00	37.296	-116.314	629	5.08_{d}^{NCSN}
HOYA^{P}	1991/09/14	19:00:00.08	37.226	-116.429	658	5.40_{L}^{NCSN}
LUBBOCK^{Y}	1991/10/18	19:12:00.00	37.063	-116.046	457	4.75_{d}^{NCSN}
BRISTOL^{Y}	1991/11/26	18:35:00.07	37.096	-116.070	457	4.80_{L}^{NCSN}
JUNCTION^{P}	1992/03/26	16:30:00.00	37.272	-116.361	622	4.82_{Lg}^{NCSN}
HUNTERS TROPHY^{R}	1992/09/18	17:00:00.08	37.207	-116.211	385	3.87_{d}^{NCSN}
DIVIDER^{Y}	1992/09/23	15:04:00.00	37.021	-115.989	340	4.13_{d}^{NCSN}
Little Skull Main	1992/06/29	10:14:21.89	36.6385	-116.2722	4530	5.31_{d}^{NCSN}
Little Skull Aftershock	1992/07/05	06:54:10.72	36.6767	-116.0178	6590	4.19_{d}^{NCSN}
Timber Mountain	1995/07/31	12:34:45.03	37.1363	-116.2057	7010	3.58_{d}^{NCSN}
Amargosa	1996/09/05	08:16:56.09	36.6827	-116.3378	5000	3.38_{d}^{NCSN}
Groom Pass	1997/04/26	01:49:35.58	37.1987	-115.9220	6040	3.72_{d}^{NCSN}
Indian Springs	1997/06/14	19:48:19.93	36.5172	-115.8133	7020	3.39_{d}^{NCSN}
Calico Fan	1997/09/12	13:36:54.20	36.8422	-116.1182	16560	3.70_{d}^{NCSN}
Warm Springs	1998/12/12	01:41:30.33	37.5437	-116.1605	2870	4.27_{d}^{NCSN}
Frenchman Flat 1	1999/01/23	03:00:34.82	36.7640	-116.0277	7410	3.45_{d}^{NCSN}
Frenchman Flat 2	1999/01/27	10:44:17.80	36.7790	-115.4578	8850	4.18_{d}^{NCSN}
Little Skull	2002/06/14	12:40:45.82	36.6438	-116.3448	8750	4.32_{d}^{NCSN}
Ralston	2007/01/24	11:30:16.10	37.4133	-117.0986	6090	4.09_{d}^{UNR}
ATRISCO Hole	1982/08/05	14:21:00	37.0842	-116.0065	640	3.50_{S}^{LNLL}
Trona Mine 1	1995/02/03	15:26:10.69	41.53	-109.64	1000	5.30_{b}^{NEIC}
Trona Mine 2	2000/01/30	14:46:51.31	41.46	-109.68	1000	4.40_{b}^{NEIC}

[1] Names in caps are NTS explosions, last three events are collapses, and all others are earthquakes.

[2] Superscript refers to NTS region where P = Pahute Mesa; R = Rainier Mesa; Y = Yucca

[3] Explosion data from Springer et al. (2002)

[4] Explosion depth of burial from Springer et al. (2002)

[5] This is the average depth of the 3 COSO shots (BRONZE, GRAY, and SILVER)

[6] Subscript refers to magnitude type and superscript refers to magnitude source

Table 2. Velocity model (Song et al., 1996)

Thick (km)	V_α (km/s)	V_β (km/s)	ρ (g/cc)	Q_α	Q_β
2.5	3.6	2.05	2.2	100.0	40.0
32.5	6.1	3.57	2.8	286.0	172.0
∞	7.85	4.53	3.3	600.0	300.0

Table 3. Event parameters ($\times 10^{20}$ dyne-cm)[1]

Name	M_W	M_{11}	M_{12}	M_{13}	M_{22}	M_{23}	M_{33}	k	-2ε
KERNVILLE	4.75	755.6	15.3	-32.6	707.1	83.4	1696.9	0.62	-0.90
AMARILLO	4.16	77.9	-21.4	29.6	156.8	28.2	191.6	0.64	0.31
DISKO ELM	3.53	9.6	-4.4	-2.8	10.2	2.1	24.2	0.58	-0.27
HORNITOS	4.72	835.1	-22.3	79.9	756.3	21.6	1516.1	0.68	-0.83
BARNWELL	4.73	548.1	-264.2	91.4	711.8	210.3	1496.6	0.59	-0.10
METROPOLIS	4.07	118.2	-3.2	0.8	139.8	-29.9	95.9	0.74	-0.08
BULLION	5.05	2043.2	-481.6	172.7	2430.5	574.9	4568.2	0.64	-0.38
AUSTIN	3.60	17.6	-6.2	0.9	15.9	4.8	28.9	0.65	0.26
HOUSTON	4.67	520.0	-72.2	-14.3	555.5	10.1	1269.2	0.62	-0.70
COSO	3.64	18.2	-2.8	5.9	26.9	-0.5	33.4	0.71	0.21
BEXAR	4.62	591.6	-139.8	43.5	792.7	-95.7	994.9	0.74	0.09
HOYA	4.75	898.1	-301.5	118.0	1034.9	9.5	1572.4	0.69	0.36
LUBBOCK	3.99	79.3	-6.3	8.7	90.1	-3.0	119.5	0.79	-0.36
BRISTOL	4.06	56.1	-21.3	19.9	101.5	-3.6	138.3	0.65	0.30
JUNCTION	4.71	592.6	-24.2	-374.2	658.7	30.8	1294.5	0.58	-0.63
HUNTERS TROPHY	3.62	14.6	-0.7	-2.8	14.9	1.8	33.4	0.62	-0.92
DIVIDER	3.65	22.5	-6.2	-0.1	30.3	3.9	31.9	0.75	0.24
Little Skull Main	5.64	3802.5	-13035.1	-8533.9	21603.9	8079.6	-34594.9	-0.08	0.02
Little Skull Aftershock	4.17	36.9	-205.6	7.5	-4.8	-3.3	9.6	0.06	-0.04
Timber Mountain	3.73	9.2	-42.9	4.0	2.6	6.9	-11.1	0.00	-0.38
Amargosa	3.69	-9.4	-2.7	-9.3	8.2	19.2	-34.7	-0.27	0.19
Groom Pass	3.76	16.2	-46.0	7.5	-3.6	-0.9	-1.5	0.07	-0.22
Indian Springs	3.57	-4.6	-24.2	0.1	-1.6	2.0	-4.6	-0.13	-0.08
Calico Fan	3.74	-8.5	-35.0	-10.5	29.6	-9.9	-5.5	0.10	-0.19
Warm Springs	4.27	-19.7	-192.6	66.7	208.8	23.1	-22.6	0.17	-0.34
Frenchman Flat 1	3.74	23.1	-21.3	-10.2	33.8	2.4	-28.3	0.19	-0.09
Frenchman Flat 2	4.65	418.0	-468.8	-154.6	893.7	47.8	-247.8	0.30	-0.47
Little Skull	4.66	50.1	-313.1	-186.6	329.9	327.6	-1145.3	-0.21	0.21
Ralston	3.85	-0.5	-66.7	16.5	13.8	13.9	-10.4	0.01	-0.09
ATRISCO Hole	4.52	-340.5	11.6	7.5	-347.3	60.2	-744.9	-0.63	0.91
Trona Mine 1	4.75	-559.1	5.8	-90.7	-548.9	-47.3	-1689.6	-0.55	0.97
Trona Mine 2	4.15	-85.0	6.7	0.9	-96.3	-6.5	-241.9	-0.60	0.80

[1] Names in caps are NTS explosions, last three events are collapses, and all others are earthquakes.
1 = North; 2 = East; 3 = Down (Aki & Richards cartesian convention).

Table 4. Velocity model perturbations

Parameter	Value
Sediment Thickness (km)	1 2.5* 4
Moho depth1 (km)	31 35* 40
Sediment V_α (km/s)	3.3 3.6* 5
Crustal V_α (km/s)	6.1* 6.202 6.485
Mantle V_α (km/s)	7.6 7.85* 8.15

* Value from Song et al. (1996)

1 The combination of sediment thicknesses and Moho depths results in crustal thicknesses of 27, 28.5, 30, 31, 32.5*, 34, 36, 37.5, and 39 km.

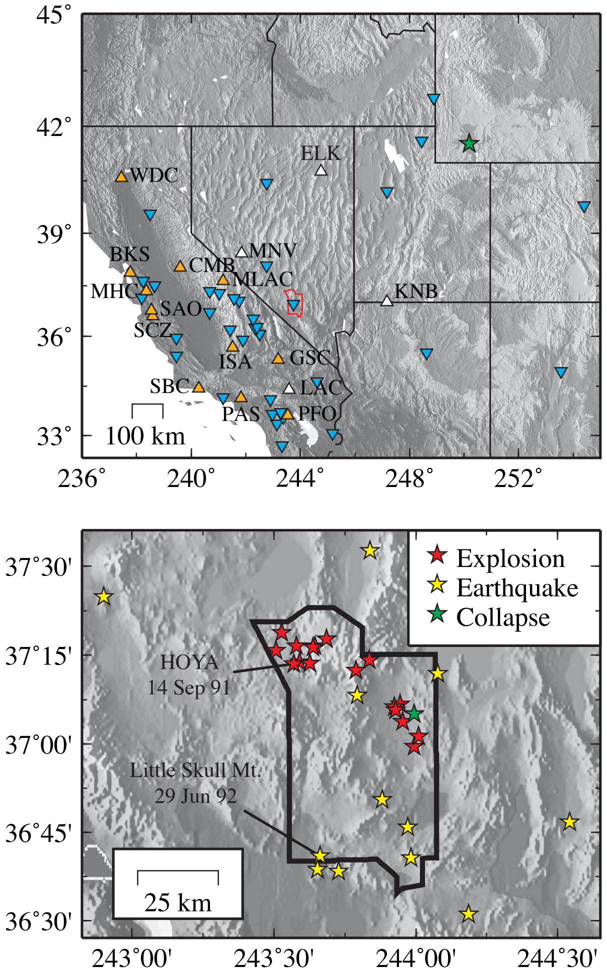

Figure 1
Ford et al., 2008
Version 1

a) Little Skull Mt. Earthquake, 29 Jun 92

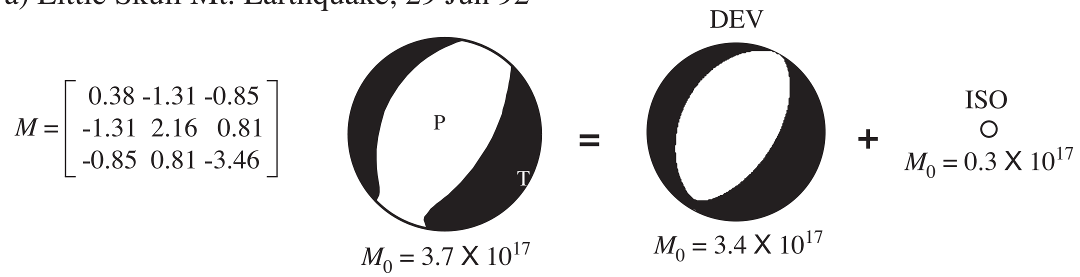

$$M = \begin{bmatrix} 0.38 & -1.31 & -0.85 \\ -1.31 & 2.16 & 0.81 \\ -0.85 & 0.81 & -3.46 \end{bmatrix}$$

b) Waveform fits

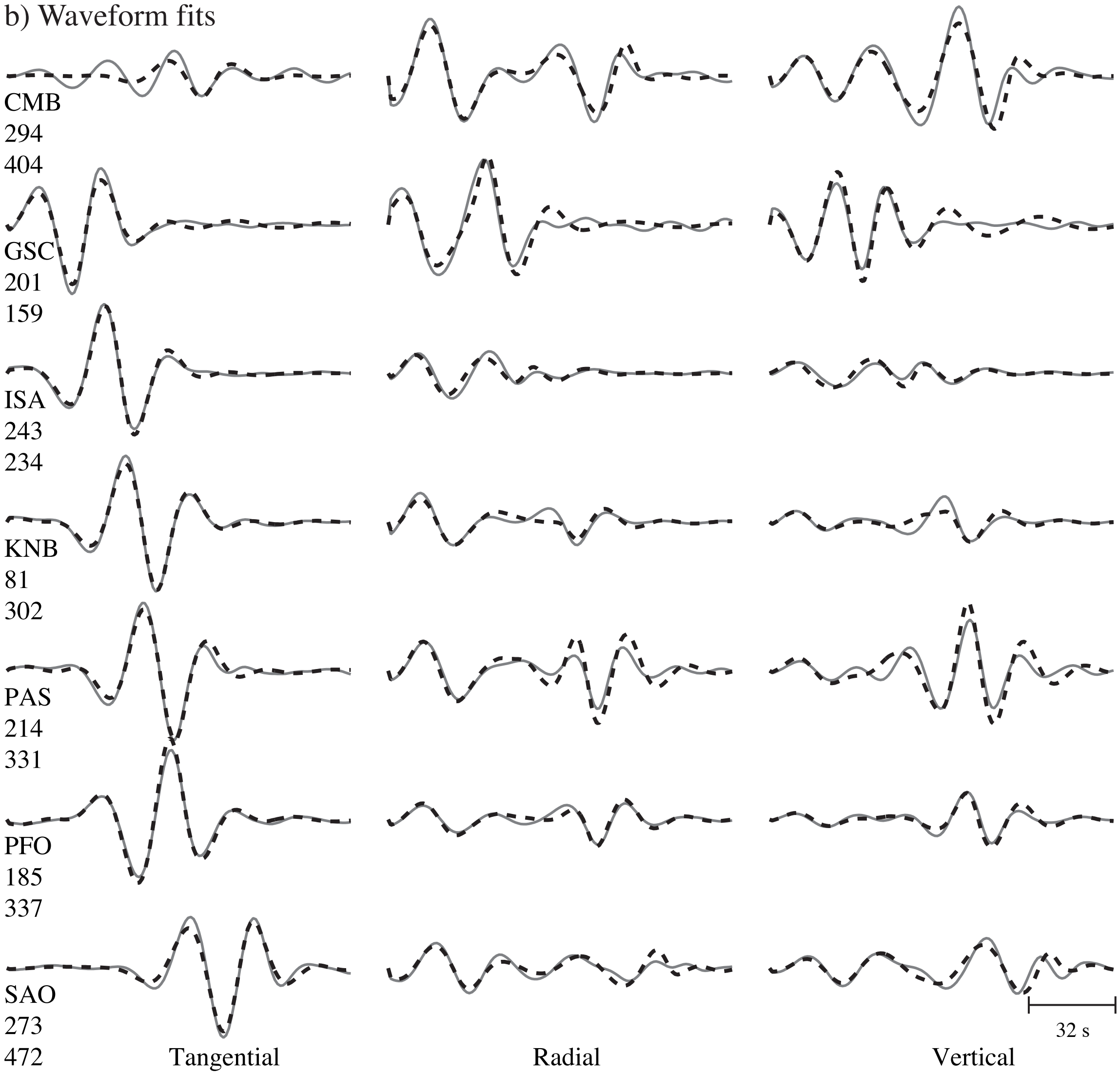

Figure 2
Ford et al., 2008
Version 1

a) HOYA Explosion, 14 Sep 91

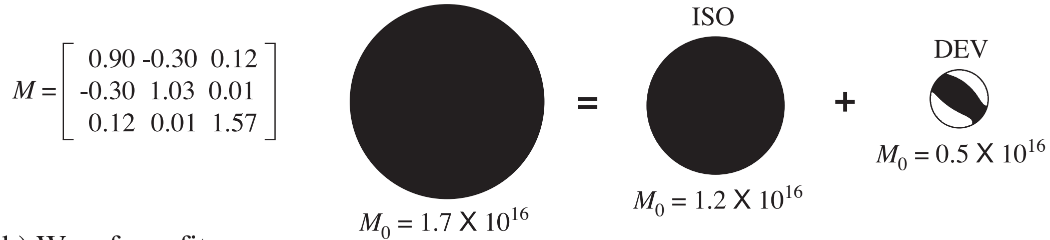

$$M = \begin{bmatrix} 0.90 & -0.30 & 0.12 \\ -0.30 & 1.03 & 0.01 \\ 0.12 & 0.01 & 1.57 \end{bmatrix}$$

b) Waveform fits

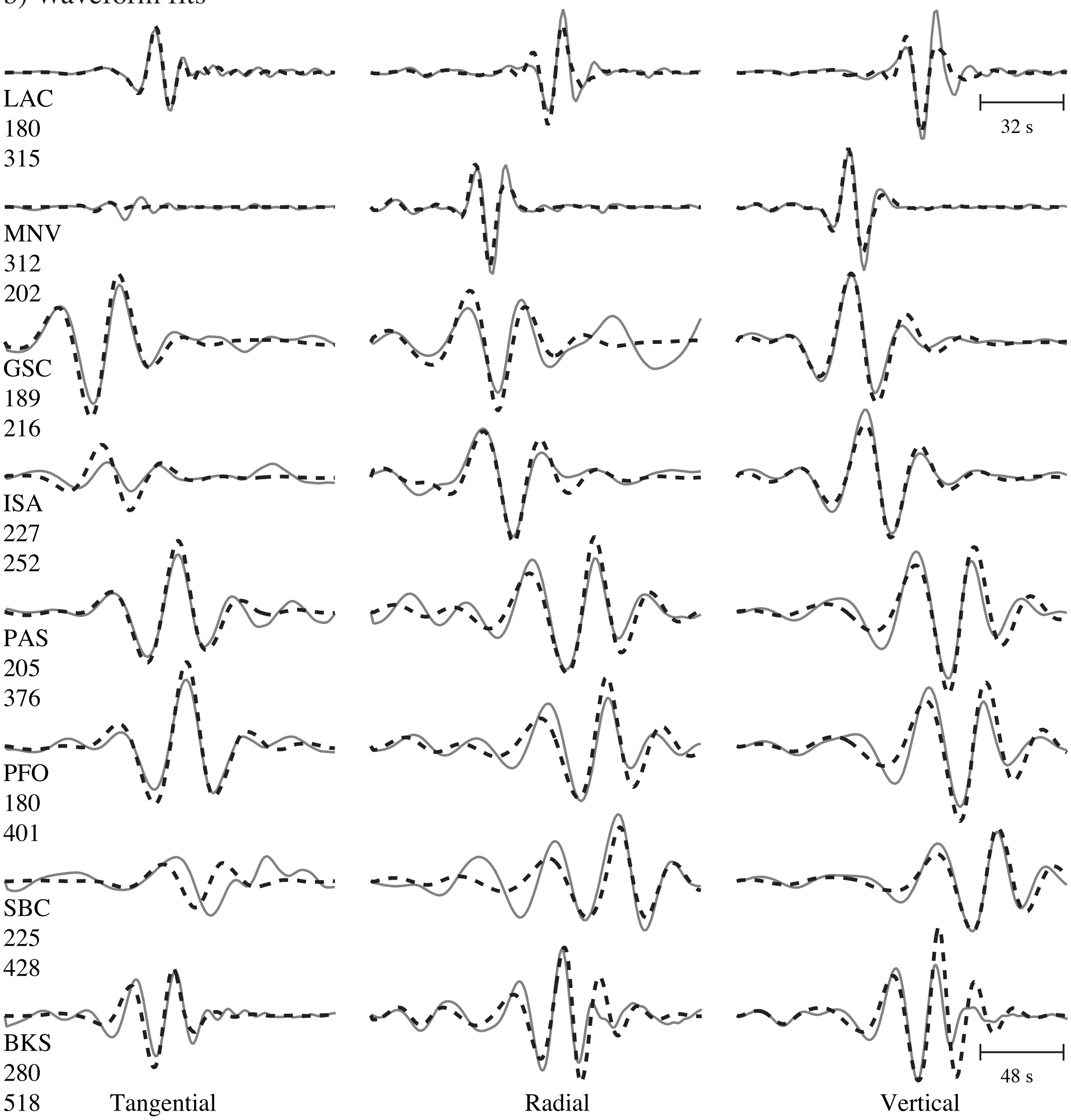

Figure 3
Ford et al., 2008
Version 1

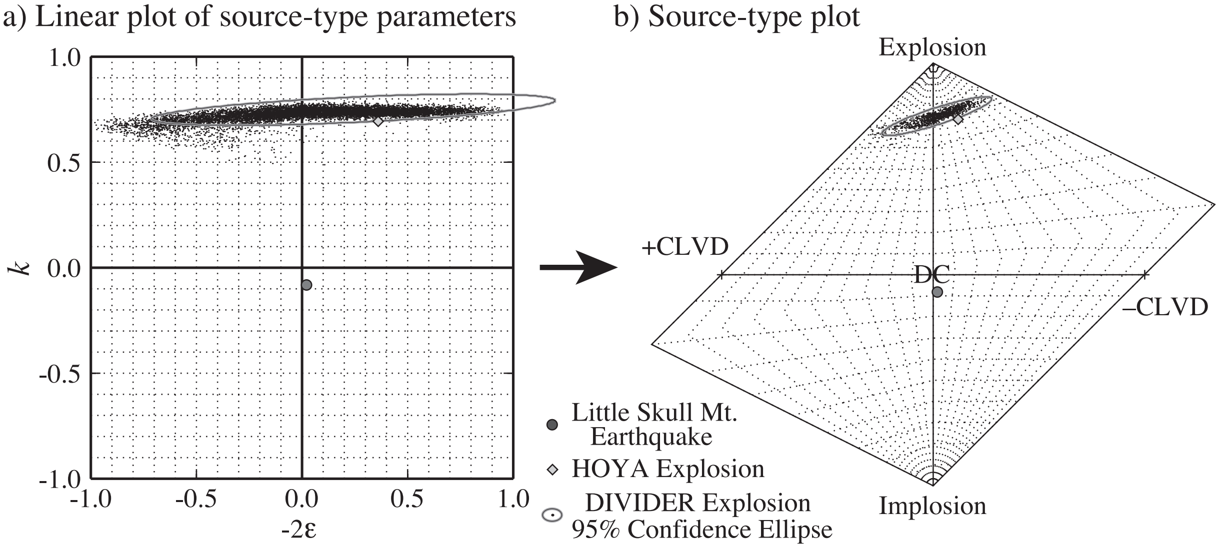

a) Linear plot of source-type parameters

b) Source-type plot

Figure 4
Ford et al., 2008
Version 3

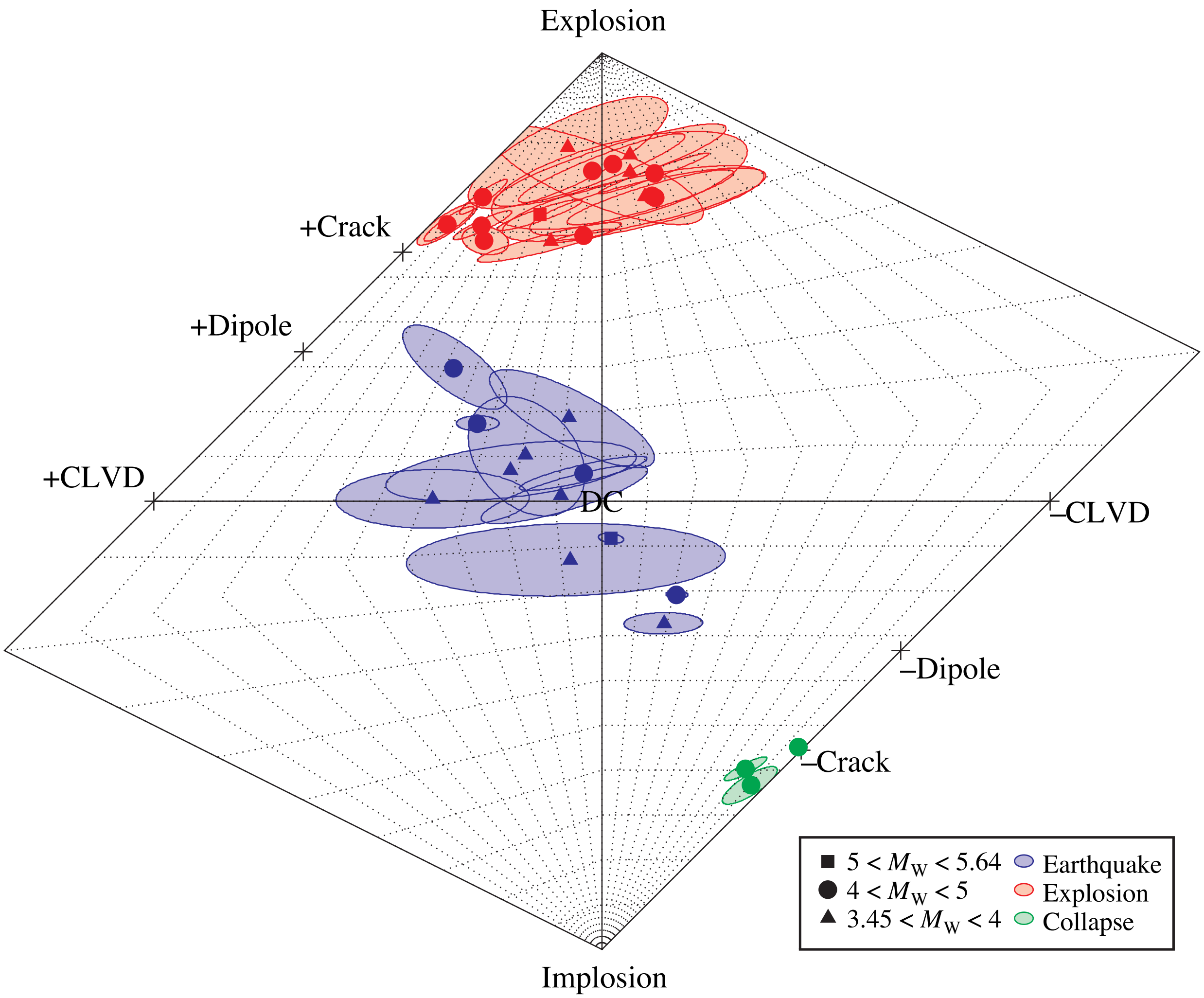

Figure 5
Ford et al., 2008
Version 1

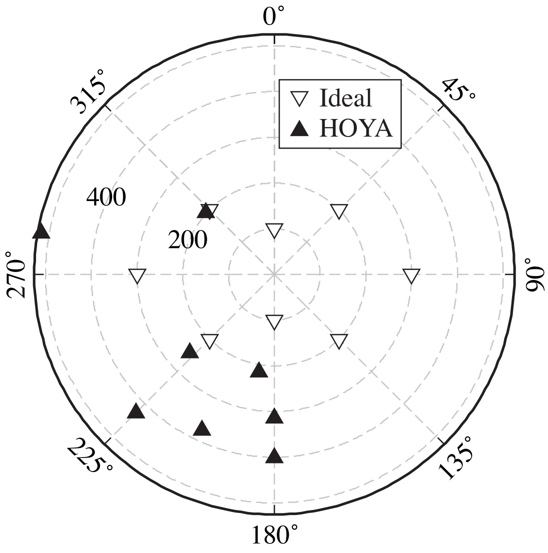

Figure 6
Ford et al., 2008
Version 1

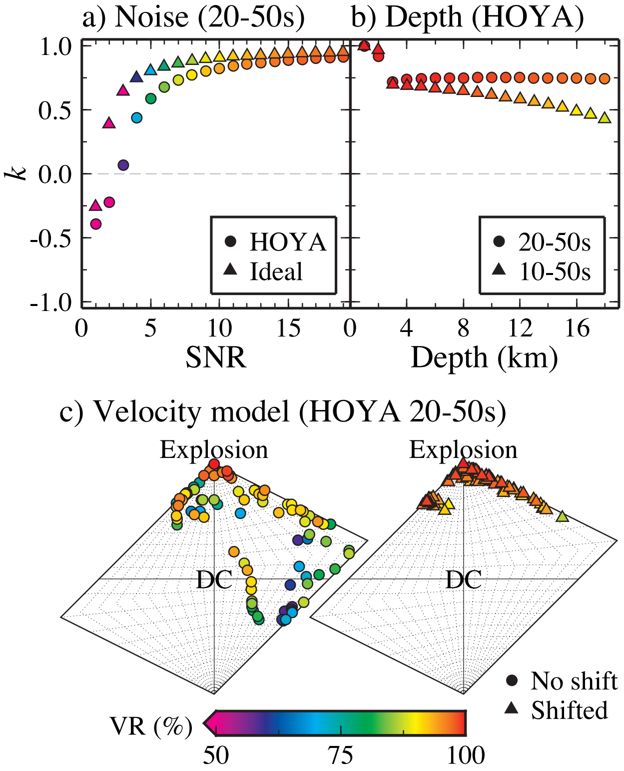

Figure 7
Ford et al., 2008
Version 1

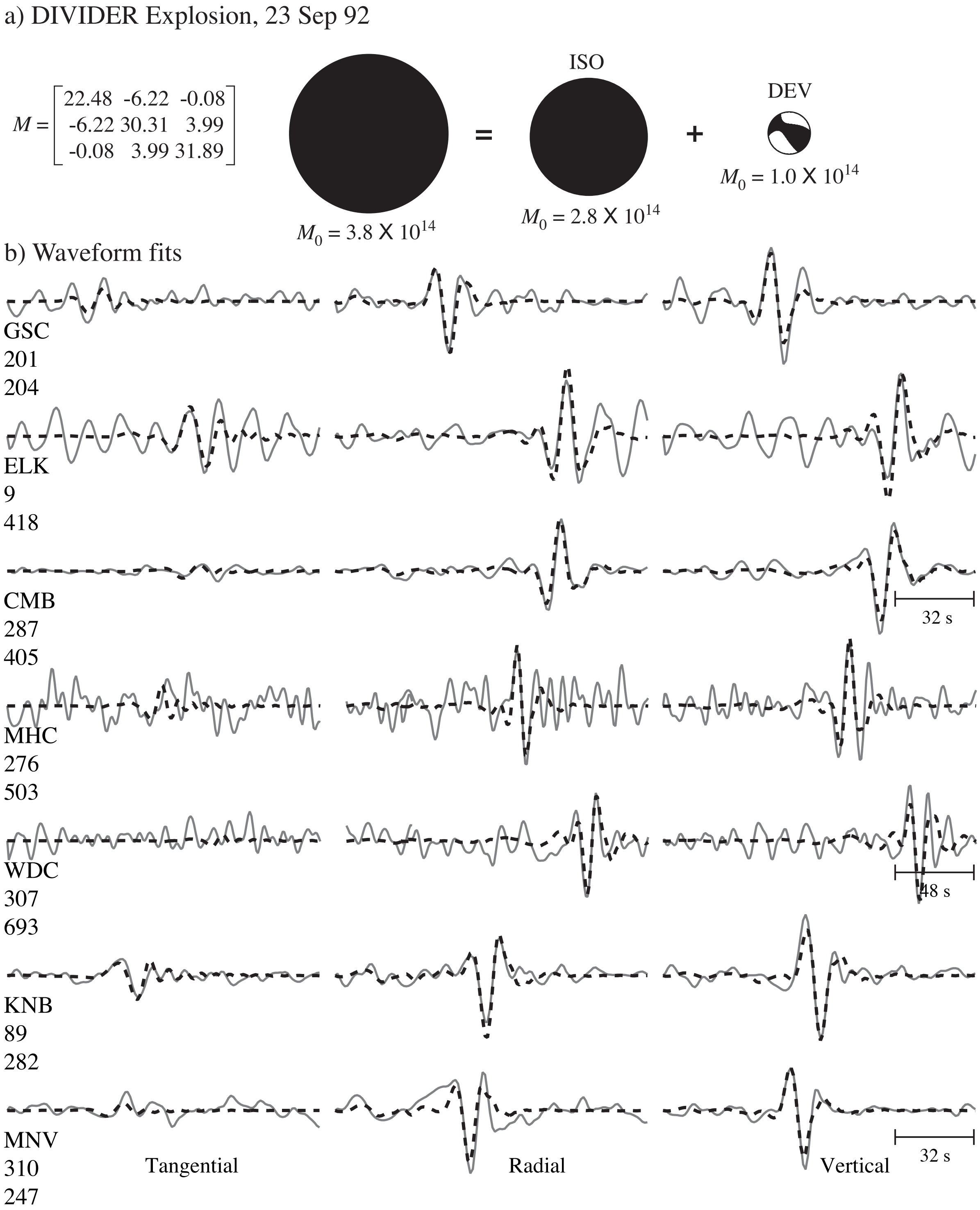

Figure 8
Ford et al., 2008
Version 1

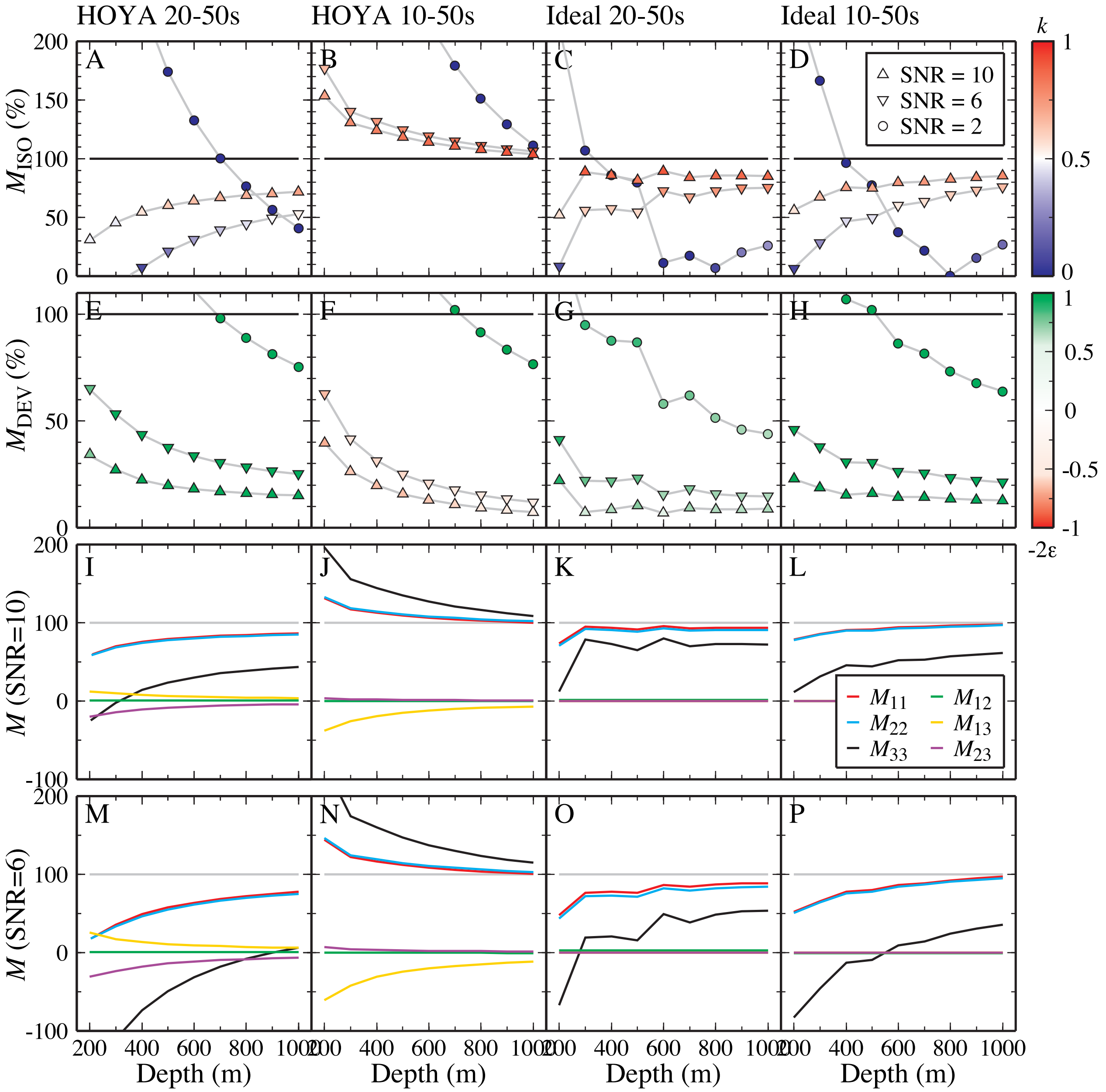

Figure 9
Ford et al., 2008
Version 1